

We are IntechOpen, the world's leading publisher of Open Access books Built by scientists, for scientists

6,900

Open access books available

186,000

International authors and editors

200M

Downloads

Our authors are among the

154

Countries delivered to

TOP 1%

most cited scientists

12.2%

Contributors from top 500 universities



WEB OF SCIENCE™

Selection of our books indexed in the Book Citation Index
in Web of Science™ Core Collection (BKCI)

Interested in publishing with us?
Contact book.department@intechopen.com

Numbers displayed above are based on latest data collected.
For more information visit www.intechopen.com



Electrified Pressure-Driven Instability in Thin Liquid Films

Hadi Nazaripoor, Adham Riad and
Mohtada Sadrzadeh

Additional information is available at the end of the chapter

<http://dx.doi.org/10.5772/intechopen.72618>

Abstract

The electrified pressure-driven instability of thin liquid films, also called electrohydrodynamic (EHD) lithography, is a pattern transfer method, which has gained much attention due to its ability in the fast and inexpensive creation of novel micro- and nano-sized features. In this chapter, the mathematical model describing the dynamics and spatiotemporal evolution of thin liquid film is presented. The governing hydrodynamic equations, intermolecular interactions, and electrostatic force applied to the film interface and assumptions used to derive the thin film equation are discussed. The electrostatic conjoining/disjoining pressure is derived based on the long-wave limit approximation since the film thickness is much smaller than the characteristic wavelength for the growth of instabilities. An electrostatic model, called an ionic liquid (IL) model, is developed which considers a finite diffuse electric layer with a comparable thickness to the film. This model overcomes the lack of assuming very large and small electrical diffuse layer, as essential elements in the perfect dielectric (PD) and the leaky dielectric (LD) models, respectively. The ion distribution within the IL film is considered using the Poisson-Nernst-Planck (PNP) model. The resulting patterns formed on the film for three cases of PD-PD, PD-IL, and IL-PD double layer system are presented and compared.

Keywords: thin liquid films, electrohydrodynamic instabilities, electrokinetic, perfect dielectric, ionic liquids, micro- and nano-patterning

1. Introduction

For the past decades, researchers and scientists have been experimenting and exploring the use of electric fields in diverse range of applications: In health and biology like treating cancer [1] and cell sorting [2], in engineering and technological applications like enhancing the heat transfer [3–6], colloidal hydrodynamics and stability [7, 8], and lithography [9]. The electric

field is defined as a force field arising from the electric charges. Depending on the nature of material (ability to polarize) and the inherent or attained surface charges, the response in the electric field varies.

Surface instabilities can be either triggered using external mechanical, thermal, and electrical forces or via intermolecular interactions like van der Waals forces [9–11]. Development of these instabilities leads to the film disruption and formation of patterns, which is of interest in many applications. In the coating and cooling processes, determining the drainage time (i.e., the time when the film breakdown occurs) and in lithography providing insight regarding different morphological structures of the film interface are few examples in numerous applications. Proper implementation of the patterning process highly depends on the knowledge of the dynamics, instability, and morphological evolution of the interface or film. Interfacial tension and viscosity of liquid film are known as dampening factors for fluctuations on the free surfaces. In small-scale systems, intermolecular forces, which depend on material properties of the substrate, liquid film, and the bounding layer, also play a dominant role in the creation and amplifying the instabilities in thin liquid films. Electrically triggered instability of thin liquid films or often call electrohydrodynamic (EHD) patterning has gained extensive attention because of its ability in the creation of micro- and nano-sized structures ranging from single and bifocal microlens arrays [12], micro and nanochannels [13], and mushroom-shaped microfibers [14].

To investigate the electrically induced instabilities of thin films, it is necessary to have an electrostatic model to find the Maxwell stress acting on the interface as a primary driving force in the system. The molten polymer film is typically assumed to be a perfect dielectric (PD), with no free charge, or a leaky dielectric (LD) which has an infinitesimal amount of charges. This requires assuming the very large and very small electric diffuse layer compared to the film thickness as the main characteristics of the PD and LD models, respectively. In the nanofilms, the film thickness is comparable to the formed diffuse layer during the evolution process which violates the PD and LD assumptions. A general model is needed to bridge the gap between PD and LD models. In ionic liquid (IL) films, with a finite amount of free charges or ions, the diffuse layer thickness is comparable to the film thickness. In this chapter, an electrostatic model is presented for different cases of PD-PD, PD-IL, and IL-PD systems to find the net electrostatic force acting on the interface. Furthermore, the spatiotemporal evolution of the interface is investigated under each condition.

2. Deriving nonlinear equation for thin film dynamics

In this part, the nonlinear governing equation is derived for the two-dimensional (2D) thin film. **Figure 1** shows the schematic of the 2D thin liquid film and bounding media sandwiched between two electrodes.

The evolution of the thin film is described using mass and momentum balances for both thin film and bounding media. The boundary conditions are a no-slip condition on the walls, no penetration (two media are immiscible), and stress balance (normal and tangent) at the interface. It is assumed that fluid is Newtonian and incompressible. Detailed mathematical representations are as follows:

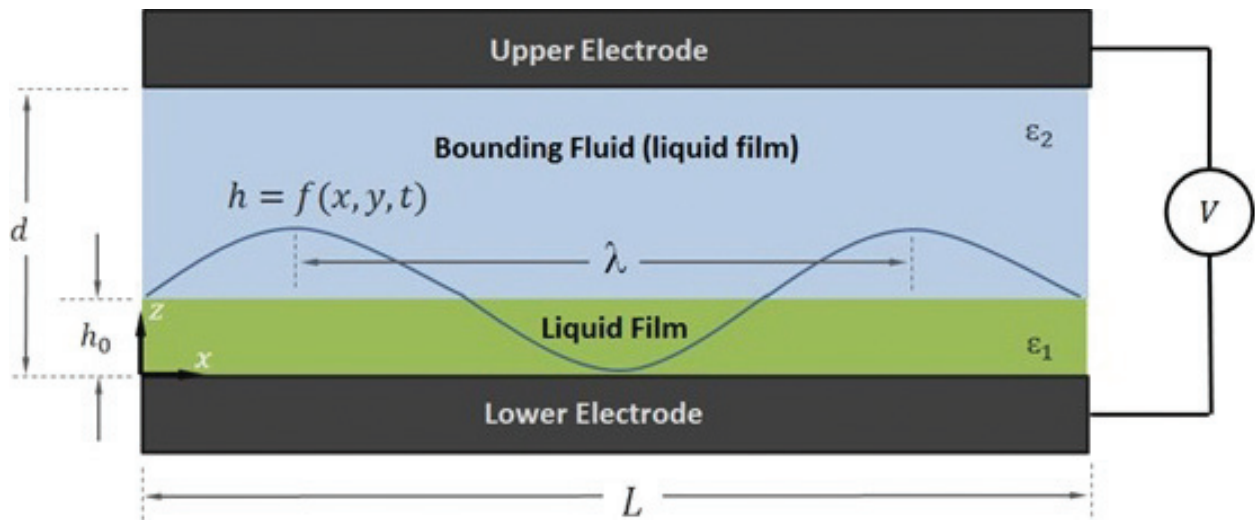


Figure 1. Schematic of the thin film sandwiched between two electrodes.

$$\rho_i \left(\frac{\partial \vec{u}_i}{\partial t} + (\vec{u}_i \cdot \nabla) \vec{u}_i \right) = -\nabla P_i + \nabla \cdot \left[\mu_i \left(\nabla \vec{u}_i + (\nabla \vec{u}_i)^T \right) \right] + \vec{f}_e \quad (1)$$

$$\nabla \cdot (\rho_i \vec{u}_i) = 0 \quad (2)$$

where $\vec{f}_e = -\nabla\phi$ accounts for external body force in which ϕ is the conjoining/disjoining pressure, μ is the dynamic viscosity, and $i = 1, 2$ denotes the i^{th} fluid phase. Here, we chose 1 for liquid film (molten polymer) and 2 for bounding media. Above equations are solved by the following boundary conditions:

$$\vec{u}_i = 0 \quad \text{at } z = 0 \quad \& \quad z = d \quad (3)$$

No slip condition and penetration at the interface:

$$\vec{u}_{\text{relative}} = 0 \quad \text{at } z = h(x, y, t) \quad (4)$$

and kinematic boundary condition for the vertical component of velocity:

$$w = \frac{\partial h}{\partial t} + u \frac{\partial h}{\partial x} + v \frac{\partial h}{\partial y} \quad \text{at } z = h(x, y, t) \quad (5)$$

Normal and tangent stress balances at the interface:

$$\vec{n} \cdot [\sigma_1 \cdot \vec{n} - \sigma_2 \cdot \vec{n}] = \kappa\gamma + \vec{f}_e \cdot \vec{n} \quad (6)$$

$$\vec{t}_i \cdot [\sigma_1 \cdot \vec{n} - \sigma_2 \cdot \vec{n}] = \vec{f}_e \cdot \vec{t}_i \quad (7)$$

where \vec{n} and \vec{t}_i are normal and tangent vectors of the interface, respectively. γ is surface tension which is assumed constant here (Note that it can vary by location) and κ is the mean

interfacial curvature of the film interface. Generally, in a 3D analysis, the film interface can be presented mathematically in the form of $G(x, y, z, t) = h(x, y, t) - z$. Using differential geometry, normal and tangent vectors and surface curvature can be found as bellow:

$$\vec{n} = n_x \vec{i}_x + n_y \vec{i}_y + n_z \vec{i}_z \quad (8)$$

$$n_x = \frac{1}{C_n} \left(\frac{\partial h}{\partial x} \right) \quad n_y = \frac{1}{C_n} \left(\frac{\partial h}{\partial y} \right) \quad n_z = \frac{-1}{C_n} \quad (9)$$

The scaling for the unit normal vector is $C_n = \sqrt{1 + \left(\frac{\partial h}{\partial x} \right)^2 + \left(\frac{\partial h}{\partial y} \right)^2}$ and the tangent vector \vec{t}_i :

$$\vec{t}_i = t^i_x \vec{i}_x + t^i_y \vec{i}_y + t^i_z \vec{i}_z \quad (10)$$

$$t^1_x = \frac{-1}{C_{t1}} \left(\frac{\partial h}{\partial y} \right) \quad t^1_y = \frac{1}{C_{t1}} \left(\frac{\partial h}{\partial x} \right) \quad t^1_z = 0 \quad (11)$$

$$t^2_x = \frac{1}{C_{t2}} \left(\frac{\partial h}{\partial x} \right) \quad t^2_y = \frac{1}{C_{t2}} \left(\frac{\partial h}{\partial y} \right) \quad t^2_z = \frac{1}{C_{t2}} \left[\left(\frac{\partial h}{\partial x} \right)^2 + \left(\frac{\partial h}{\partial y} \right)^2 \right] \quad (12)$$

The scaling for the tangent vectors are $C_{t1} = \sqrt{\left(\frac{\partial h}{\partial x} \right)^2 + \left(\frac{\partial h}{\partial y} \right)^2}$ and $C_{t2} = \sqrt{\left(\frac{\partial h}{\partial x} \right)^2 + \left(\frac{\partial h}{\partial y} \right)^2 + \left(\left(\frac{\partial h}{\partial x} \right)^2 + \left(\frac{\partial h}{\partial y} \right)^2 \right)^2}$.

Finally, the surface curvature which is presented by two principle radii of curvature R_1 and R_2 is given by:

$$\kappa = \left(\frac{1}{R_1} + \frac{1}{R_2} \right) \quad (13)$$

Principle radii of curvature for the interface can be defined based on the film thickness as:

$$\frac{1}{R_1} + \frac{1}{R_2} = \frac{\frac{\partial^2 h}{\partial x^2} \left(1 + \left(\frac{\partial h}{\partial y} \right)^2 \right) + \frac{\partial^2 h}{\partial y^2} \left(1 + \left(\frac{\partial h}{\partial x} \right)^2 \right) - 2 \frac{\partial^2 h}{\partial x \partial y} \frac{\partial h}{\partial x} \frac{\partial h}{\partial y}}{\left(1 + \left(\frac{\partial h}{\partial x} \right)^2 + \left(\frac{\partial h}{\partial y} \right)^2 \right)^{\frac{3}{2}}} \quad (14)$$

In the case of 2D analysis, $G(x, z, t) = h(x, t) - z$, above relations are simplified as follows:

$$n_x = \frac{1}{C_n} \left(\frac{\partial h}{\partial x} \right); \quad n_y = 0; \quad n_z = \frac{-1}{C_n}; \quad C_n = \sqrt{1 + \left(\frac{\partial h}{\partial x} \right)^2} \quad (15)$$

$$t^1_x = 0 \quad t^1_y = \frac{1}{C_{t1}} \left(\frac{\partial h}{\partial x} \right) \quad t^1_z = 0 \quad (16)$$

$$t_x^2 = \frac{1}{C_{t2}} \left(\frac{\partial h}{\partial x} \right)^2 \quad t_y^2 = 0 \quad t_z^2 = \frac{1}{C_{t2}} \left(\frac{\partial h}{\partial x} \right)^2 \quad (17)$$

$$C_{t1} = \left| \frac{\partial h}{\partial x} \right| \quad \& \quad C_{t2} = \left| \frac{\partial h}{\partial x} \right| \sqrt{1 + \left(\frac{\partial h}{\partial x} \right)^2}; \quad \kappa = \frac{\frac{\partial^2 h}{\partial x^2}}{\left(1 + \left(\frac{\partial h}{\partial x} \right)^2 \right)^{\frac{3}{2}}} \quad (18)$$

Hence, normal and tangent components of stress balance Eqs. (6) and (7) for the film in the 2D case are given by

$$\begin{aligned} -(p_1 - p_2) + \frac{2\mu_1 h_x}{1 + h_x^2} [-(u_{1z} + w_{1x}) + r(u_{2z} + w_{2x})] + \frac{2\mu_1 (1 - h_x^2)}{1 + h_x^2} [w_{1z} - r w_{2z}] \\ = \frac{h_{xx}}{(1 + h_x^2)^{\frac{3}{2}}} \gamma \end{aligned} \quad (19)$$

$$(1 - h_x^2)[(u_{1z} + w_{1x}) - r(u_{2z} + w_{2x})] + 2h_x[(w_{1z} - u_{1x}) - r(w_{2z} - u_{2x})] = 0 \quad (20)$$

where $r = \frac{\mu_2}{\mu_1} \ll 1$ is the bounding media to film dynamic viscosity ratio which is the small quantity in our case. For instance, water viscosity at 25° C is 0.894 [mPa.s or cP] and for castor oil is 985 [mPa.s or cP]. Therefore, the bounding media can be considered as an inactive media and there is no need to solve the evolution equations (Navier–Stokes and continuity) for both media. Also, as film thickness $h_0 \ll 1$, inertial effects are negligible ($Re \ll 1$, creeping flow). Here and thereafter, we just consider film evolution equations and do not use the subscript 1 for the film velocity components.

The subscripts in above equations \square_x and \square_z represent derivatives with respect to x and z , respectively. In what follows, scaling parameters are used to nondimensionalize governing equations and boundary conditions (capital letters are dimensionless):

$$x = \lambda X \quad y = \lambda Y \quad z = h_0 Z \quad u = u_0 U \quad v = u_0 V \quad (21)$$

where λ is the maximum wavelength of the surface instabilities, h_0 is the initial thickness of the film, u_0 is the maximum value of lateral velocity, and k is defined as $k = \frac{h_0}{\lambda}$. By using definitions in Eq. (21) and applying to mass continuity equation Eq. (2):

$$w = u_0 k W \quad (22)$$

Time is also re-scaled by employing long length scale λ and characteristic velocity u_0

$$t = \frac{h_0}{k u_0} T \quad (23)$$

As a result of the long wave approximation theory $k = \frac{h_0}{\lambda} \ll 1$, flow within the film is locally parallel [15]. Pressure and conjoining/disjoining pressure are scaled as

$$(p, \phi) = \frac{kh_0}{\mu_1 u_0} (P, \Phi) \quad (24)$$

(P, Φ) are dimensionless pressure and conjoining/disjoining pressure.

Stress balance in normal direction, Eq. (19), can be written in the scaled form as follows:

$$\begin{aligned} & -(P_1 - P_{ext}) + \frac{2H_X}{1 + k^2 H_X^2} k^2 [-(U_Z + kW_X)] + \frac{2(1 - k^2 H_X^2)}{1 + k^2 H_X^2} [k^2 W_Z] \\ & = \left(\frac{H_{XX}(1 + k^2 H_{YY}) + H_{YY}(1 + k^2 H_{XX}) - 2k^4 H_{XY} H_X H_Y}{(1 + k^2 H_X^2 + k^2 H_Y^2)^{\frac{3}{2}}} \right) \frac{k^3 \gamma}{\mu_1 u_0} \end{aligned} \quad (25)$$

and in tangential direction, Eq. (20), is scaled as below:

$$(1 - k^2 H_X^2) [U_Z + k^2 W_X] + 2k^2 H_X [W_Z - U_X] = 0 \quad (26)$$

where P_{ext} represents scaled form of p_2 in Eq. (19). $P_1 - P_{ext}$ can be called gage pressure (P) without loss of generality. Rewriting Navier–Stokes and mass continuity equations, Eqs. (1) and (2), by using above definitions we have,

$$kRe(U_T + UU_X + VU_Y + WU_Z) = -(P + \Phi)_X + k^2(U_{XX} + U_{YY}) + U_{ZZ} \quad (27)$$

$$kRe(V_T + UV_X + VV_Y + WV_Z) = -(P + \Phi)_Y + k^2(V_{XX} + V_{YY}) + V_{ZZ} \quad (28)$$

$$kRe(W_T + UW_X + VW_Y + WW_Z) = -(P + \Phi)_Z + k^4(W_{XX} + W_{YY}) + k^2 W_{ZZ} \quad (29)$$

$$U_X + W_Z = 0 \quad (30)$$

and boundary conditions, Eqs. (3) and (5),

$$\vec{U}_i = 0 \quad \text{at} \quad Z = 0 \quad \& \quad Z = \frac{d}{h_0} \quad (31)$$

$$W = \frac{\partial H}{\partial T} + U \frac{\partial H}{\partial X} \text{ at } Z = H(X, T) \quad (32)$$

In the EHD pattern evolution process, the electric field destabilizes the interface of the fluids, causing the interface deformation with the height of $h = f(x, y, t)$. The characteristic wavelength of the growing instabilities, λ , is much larger than the initial film thickness ($k \ll 1$), so a “long-wave approximation” [16] is used to simplify the governing equations. To avoid losing the effects of interfacial tension, this assumption is made: $k^3 \gamma = O(1)$.

$$(P + \Phi)_X = U_{ZZ} \quad (33)$$

$$(P + \Phi)_Z = 0 \quad (34)$$

$$U_X + W_Z = 0 \quad (35)$$

$$-P = H_{XX} \text{ at } Z = H(X, T) \quad (36)$$

$$U_Z = 0 \quad \text{at } Z = H(X, T) \quad (37)$$

$(P + \Phi)$ is called modified pressure (\bar{P}). Eq. (34) shows that, the modified pressure does not change across the film thickness. From Eq. (31), (33), and (37), velocity component U is found as follows:

$$U = \bar{P}_X Z \left(\frac{1}{2} Z - H \right) \quad (38)$$

Using Eqs. (38) and (35) leads to velocity component W,

$$W = \frac{1}{2} Z^2 \left[-\frac{1}{3} Z (\bar{P}_{XX}) + (\bar{P}_X H)_X \right] \quad (39)$$

Substituting velocity component values U and W that are evaluated at $Z = H(X, T)$ into Eq. (32) gives the film evolution equation:

$$H_T - \left[\frac{H^3}{3} \bar{P}_X \right]_X = 0 \quad (40)$$

Replacing the modified pressure with pressure and conjoining/disjoining pressure, then using Eq. (36) for pressure results in the following thin film equation,

$$H_T + \frac{\partial}{\partial X} \left[H^3 \frac{\partial \Psi}{\partial X} \right] = 0 \quad (41)$$

$$\Psi = \frac{1}{3} (H_{XX} - \Phi)$$

and in a two-dimensional form and considering y-direction,

$$\mu h_t + \frac{\partial}{\partial x} \left[h^3 \frac{\partial \psi}{\partial x} \right] + \frac{\partial}{\partial y} \left[h^3 \frac{\partial \psi}{\partial y} \right] = 0 \quad (42)$$

$$\psi = \frac{1}{3} (\gamma (h_{xx} + h_{yy}) - \phi)$$

2.1. Interaction potentials

Conjoining pressure, ϕ , (force acting on the film interface per unit area) is defined as the gradient of excess intermolecular interactions, $\phi = \nabla(\Delta G)$. In EHD, the electric field induces a pressure at the film interface, which is added to the natural interactions to generate excess intermolecular interactions. The conjoining pressure, ϕ , is a summation of these interaction potentials: van der Waals, electrostatic, and Born repulsive interaction potentials and is given as:

$$\phi = \phi_{vdW} + \phi_{Br} + \phi_{EL} \quad (43)$$

The van der Waals interaction is the summation of Keeson, Debye, and London dispersion forces [17, 18]. This interaction is defined as $\phi_{vdW_L} = A_L/6\pi h^3$ and $\phi_{vdW_U} = -A_U/6\pi(d-h)^3$ for the

lower and upper electrodes, respectively. A_L and A_U are effective Hamaker constant lower and upper electrodes, which depend on the materials used for electrodes and fluid layers. For instance, for three-layered systems, it is defined: $A_{213} = (\sqrt{A_{33}} - \sqrt{A_{11}}) (\sqrt{A_{22}} - \sqrt{A_{11}})$ in which 1, 2, and 3 denote substrate, liquid film, and bounding fluid, respectively.

The van der Waals interaction becomes singular as $h \rightarrow 0$ and $h \rightarrow d$. To avoid nonphysical penetration of liquid to solid phase, in case of film rupture and touching, a cutoff distance, l_0 , is defined for which a short-range repulsive force, called Born repulsion, acts on the film interface [19]. This is used to maintain a minimum equilibrium liquid thickness on both electrodes and is defined as $\phi_{BrL} = -8B_L/h^9$ and $\phi_{BrU} = 8B_U/(d-h)^9$ for the lower and upper electrodes, respectively. Coefficients B_L and B_U are found by setting the net conjoining pressure equal to zero at $h = l_0$ and $h = d - l_0$ for lower and upper surfaces.

The electrostatic conjoining/disjoining pressure depends on the electrostatic property of liquid thin film and bounding layer, which is discussed in the following sections. Throughout this study, it is assumed that electric breakdown does not occur during the EHD patterning process.

2.2. Numerical scheme

Different numerical methods are used to track the free interfaces [20, 21], and particularly, in the EHD patterning process [22–25]. The numerical methods are applied as versatile tools to monitor and visualize the transient evolution of liquid film subject to an electric field. Here, the thin film equation, Eq. (42) is solved numerically to obtain the transient behavior using finite difference method and adaptive time step solver. More details about the numerical scheme are available in [26].

3. Perfect dielectric film and bounding media

In this part, we consider the film and bounding media as two perfect dielectric media and solve Laplace equation in 1D. Governing equations and applied boundary conditions [27–29] are as follows:

$$\nabla^2 \psi_i = 0 \quad (44)$$

$$\psi_1 = \psi_{low} \text{ at } z = 0 \quad (45)$$

$$\psi_1 = \psi_2 \text{ at } z = h(x, y, t) \quad (46)$$

$$\left(\vec{n} \cdot \varepsilon \vec{D} \right)_1 - \left(\vec{n} \cdot \varepsilon \vec{D} \right)_2 = 0 \text{ at } z = h(x, y, t) \quad (47)$$

$$\psi_2 = 0 \quad \text{at } z = d \quad (48)$$

Solving Eq. (44) with mentioned boundary conditions give rise to electric potential distribution across the domain as follows:

$$\psi_1 = \frac{\varepsilon_2}{\varepsilon_1} \left[\frac{-\psi_{low}}{h \left(\frac{\varepsilon_2}{\varepsilon_1} - 1 \right) + d} \right] z + \psi_{low} \quad (49)$$

$$\psi_2 = \left[\frac{-\psi_{low}}{h \left(\frac{\varepsilon_2}{\varepsilon_1} - 1 \right) + d} \right] (z - d) \quad (50)$$

The *Maxwell stress* tensor is defined as follows:

$$T = \varepsilon \begin{bmatrix} E_x^2 - \frac{1}{2} E^2 & E_x E_y & E_x E_z \\ E_y E_x & E_y^2 - \frac{1}{2} E^2 & E_y E_z \\ E_z E_x & E_z E_y & E_z^2 - \frac{1}{2} E^2 \end{bmatrix}$$

where E is defined as $E^2 = E_x^2 + E_y^2 + E_z^2$ and electric field components can be found as follows:

$$E_x = -\frac{\partial \psi}{\partial x} \quad E_y = -\frac{\partial \psi}{\partial y} \quad E_z = -\frac{\partial \psi}{\partial z} \quad (51)$$

Traction force vector acting on the interface because of *Maxwell stress* is found as follows:

$$\vec{F} = \int_S (\vec{n} \cdot \vec{T}) dS \quad (52)$$

where S is the interface area and \vec{n} is the unit normal vector of the interface.

$$\vec{n} = n_x \vec{i}_x + n_y \vec{i}_y + n_z \vec{i}_z$$

where \vec{n} is the unit normal vector into the medium. In the long-wave limit approximation, the traction forces for each layer are given as:

$$\vec{F}_1 = -\frac{1}{2} \varepsilon_1 E_{1z}^2 S \vec{i}_z \quad (53)$$

$$\vec{F}_2 = \frac{1}{2} \varepsilon_2 E_{2z}^2 S \vec{i}_z \quad (54)$$

Therefore, the net force per unit area, conjoining pressure is

$$\phi_{ES} = -\frac{1}{2} \varepsilon_1 \left(\frac{\varepsilon_1}{\varepsilon_2} - 1 \right) \left[\frac{\psi_{low}}{\frac{\varepsilon_1}{\varepsilon_2} d - h \left(\frac{\varepsilon_1}{\varepsilon_2} - 1 \right)} \right]^2 \quad (55)$$

The net electrostatic force acting on the interface depends on the electric permittivity of each layer, applied potential, electrodes separation distance, and interface height.

3D snapshots were plotted to investigate the effect that a transverse electric field has on the nondimensional structural height variations over time of a PD film, with an initial thickness of 30 nm. **Figure 2(a)** shows the formation of small random disturbances in the liquid film that are conical in shape. These evolve with time as liquid flows from regions of lower thickness to regions of higher thickness causing them to increase in size and length and become more pillar-shaped as shown in **Figure 2(b)**. However, once the pillars reach the upper electrode, their height ceases to increase, and the pillars begin to increase their cross-sectional area, as shown in **Figure 2(c)**.

A detailed spatiotemporal evolution for the liquid–liquid interface instabilities in a 2D domain highlighting the different patterns formation using different initial film thickness is presented in **Figure 3**. The relative electric permittivity ratio of bilayer system is 0.6 and the initial lower layer film thickness is increased from 20 nm to 85 nm. As a result, four patterns of pillars, bicontinuous, holes, and roll-like features are formed. At lower thickness, 20 nm, pillars are formed (image a(ii)) but merging of neighbor pillars results in coarse final structure (image a(iii)). Bicontinuous structures are formed when the film thickness is increased to 50 nm (image b(i–iv)) which is not desired. The bicontinuous structures behave similarly to an air-in-liquid dispersion that also takes place in air-polymer systems with high filling ratios. The further increase in the film thickness leads to a columnar holes formation in the film (images c(i–iv)). In very thick films, 75 nm, the role-like features form that are spaced with micrometer distance. This type of features can be used as nanochannels in practical applications. The roll-like structures, in d(i), seem to be an organized version of the bicontinuous structures generated by the same phase inversion mechanism shown in b(i).

In the EHL process, both the initial layer thickness and electric permittivity ratio play an important role in the process and can develop different patterns on the film. **Figure 4** shows the different types of patterns formed as a function of the relative electric permittivity ratios of layers ' ϵ_r ' and nondimensional initial mean film thickness of h_0/d , in a liquid–liquid interface. As shown in **Figure 4**, changing the electric permittivity ratios may lead to having two to four kinds of structures depending on the initial layer thickness. In electric permittivity ratios greater than one, two main shapes of structures form, pillars in filling ratios (h_0/d) less than 0.5 and bicontinuous structures in relatively thicker films. However, as shown in **Figure 4**, in electric permittivity ratios less than one, four different shapes of structures can form. The generated map shown in **Figure 4** provides details about the threshold values of the filling ratio in which the transition between structures happens at different electric permittivity ratios. From thermodynamics, the shape that leads to the lowest free energy in the system

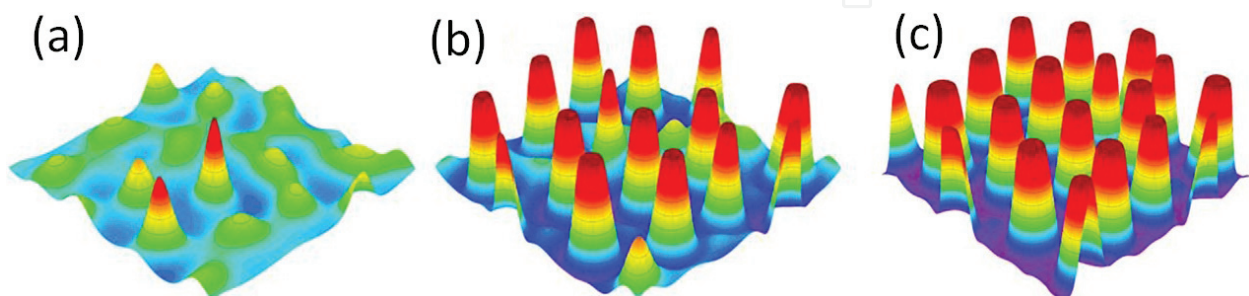


Figure 2. PD film with $h_0 = 30 \text{ nm}$, 3D spatiotemporal evolution of a PD liquid PD film (images a–c). Nondimensional times, T are: (a) 3×10^5 (b) 3.5×10^5 (c) 4.5×10^5 .

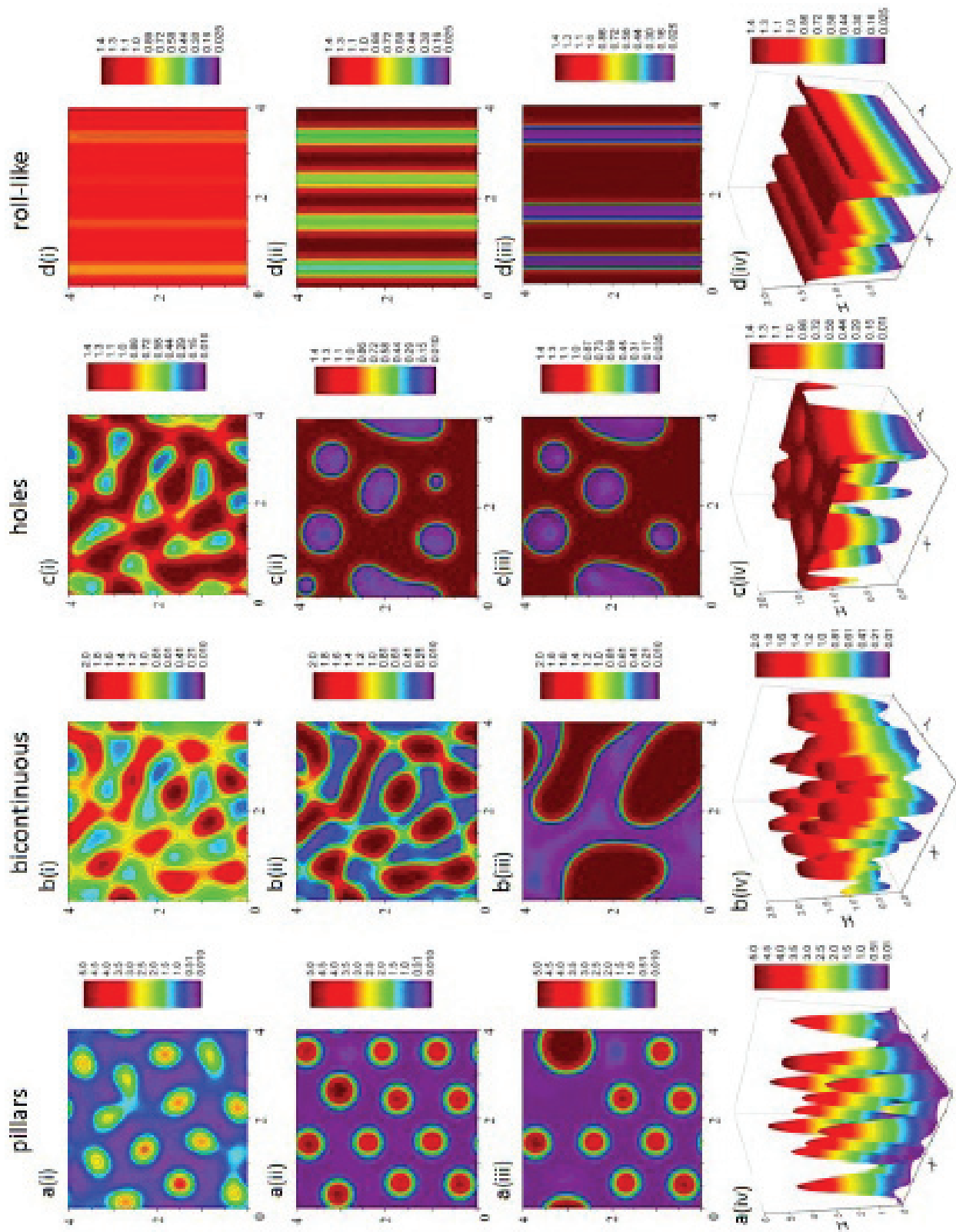


Figure 3. Base case PD-PD bilayer, (a–d) images from i to iii show the 2D spatiotemporal evolution for liquid–liquid interface instabilities in a 2 domain when $\epsilon_r = 0.6$ and $\ell_l = 2.5$. Initial mean film thicknesses (h_0) are: A(i–iv) 20 nm, b(i–iv) 50 nm, c(i–iv) 70 nm, and d(i–iv) 85 nm. Initial electric field intensities (E_0) are 294, 250, 227, and 212 MV/m, respectively. Reprinted with permission from (HADI NAZARIPOOR et al. LANGMUIR 2014, 30, 14734–14744). Copyright (2014) American Chemical Society.

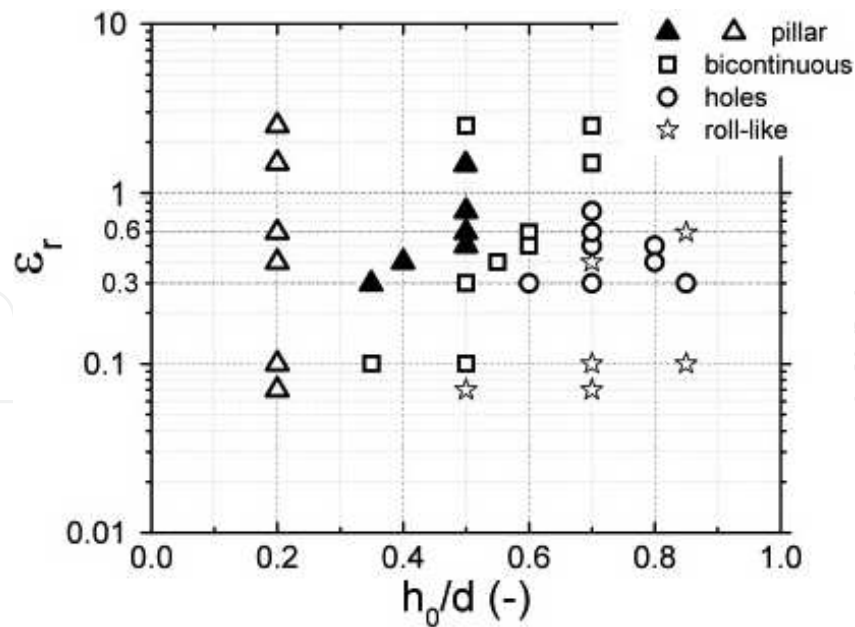


Figure 4. A parametric map that shows the different types of patterns formed, in 2D, as a function of the relative electric permittivity ratios of layers ' ϵ_r ' and nondimensional initial mean film thickness of h_0/d , in a liquid–liquid interface. Reprinted with permission from (HADI NAZARIPOOR et al. LANGMUIR 2014, 30, 14734–14744). Copyright (2014) American Chemical Society.

determines the final pattern. **Figure 4** also shows that there is a critical initial film thickness for each value of ϵ_r , where below it only pillars are formed.

4. Perfect dielectric film and ionic conductive bounding media

In this section, an ionic conductor is chosen as a bounding media and a dielectric media for thin film, for instance, salt water–oil system. Saltwater behaves like conductors due to having free ions, so Poisson equation is solved to find the electric potential distribution over the domain, and for the oil part similar to the previous section, Laplace equation is considered. Detailed mathematical procedure is

$$\epsilon_i \nabla^2 \psi_i = -\rho_{f_i} \quad (56)$$

$$\psi_1 = 0 \quad \text{at } z = 0 \quad (57)$$

$$\psi_1 = \psi_2 \quad \text{at } z = h(x, y, t) \quad (58)$$

$$\left(\vec{n} \cdot \epsilon \vec{D} \right)_1 - \left(\vec{n} \cdot \epsilon \vec{D} \right)_2 = 0 \quad \text{at } z = h(x, y, t) \quad (59)$$

$$\psi_2 = \psi_{up} \quad \text{at } z = d \quad (60)$$

The space charge density of the mobile ions ρ_f is zero for dielectric media as they do not have any ions, but for the IL, ρ_{f_2} is given by [18],

$$\rho_{f2} = \sum_{i=1}^N z_i e n_{i\infty} \exp\left(-\frac{z_i e (\psi - \psi_{\infty})}{k_B T}\right) \quad (61)$$

Eq. (61) is called the Boltzmann distribution. Here, z_i is the valence of species i , e is the magnitude of electron charge, 1.602×10^{-19} (C), $n_{i\infty}$ is the bulk ionic number concentration (say, in m^{-3}), N is the number of species in the electrolyte, k_B is the Boltzmann constant, 1.378×10^{-23} (J/K), and T is the temperature in (K).

Ionic number concentration, n_{∞} , is given by

$$n_{\infty} = 1000 N_A M$$

with Avogadro number, $N_A = 6.022 \times 10^{23} \text{ mol}^{-1}$ and M being the electrolyte molar concentration (mol/L).

Proof

Generally, ρ_f is defined based on ionic number concentration n_i of species i^{th} as follows:

$$\rho_f = \sum_{i=1}^N z_i e n_i \quad (62)$$

Ionic number concentration, n_i , near a charged surface can be found by considering ion conservation Eq. (63) for the steady-state and equilibrium condition which leads to zero-ion flux, $\vec{j}_i = 0$. Here, R_i represents for reactions that produce/consume species i in the electrolyte and set to zero.

$$\frac{\partial n_i}{\partial t} = -\nabla \cdot \vec{j}_i + R_i \quad (63)$$

Ion flux, \vec{j}_i , for species i , is defined by the Nernst-Planck relationship Eq. (64)

$$\vec{j}_i = n_i \vec{u} - D_i \nabla n_i - \frac{z_i e n_i D_i}{k_B T} \nabla \psi \quad (64)$$

At the equilibrium, there is no fluid velocity, $\vec{u} = 0$, so for the 1D case (z-direction) it is simplified as follows:

$$\frac{dn_i}{dz} + \left(\frac{z_i e n_i}{k_B T}\right) \frac{d\psi}{dz} = 0 \quad (65)$$

Eq. (65) has an analytical solution with the following boundary conditions:

$$n_i = n_{i\infty} \text{ and } \psi = \psi_{\infty} \text{ at } |z| \gg 0 \quad (66)$$

$$n_i = n_i \text{ and } \psi = \psi \text{ at } |z| = 0 \quad (67)$$

where $|z|$ shows distance from charged surface, ψ_∞ and $n_{i\infty}$ are bulk (electro neutral) electric potential and ion number concentration, respectively. ψ_{∞_i} is also called reference potential, ψ_{ref} . From now we use ψ_{ref} instead of ψ_∞ . By using Eqs. (66) and (67), the solution is:

$$n_i = n_{i\infty} \exp \left[- \frac{z_i e (\psi - \psi_{ref})}{k_B T} \right] \quad (68)$$

Substituting Eq. (68) into Eq. (62) results in Eq. (61).

Proof. end

Using Boltzmann distribution (relation Eq. (61)) for the free space charge density, ρ_f , in the Poisson Eq. (56) give rise to well-known Poisson-Boltzmann (PB) equation

$$\varepsilon_2 \nabla^2 \psi_2 = - \sum_{i=1}^N z_i e n_{i\infty} \exp \left(- \frac{z_i e (\psi_2 - \psi_{ref})}{k_B T} \right) \quad (69)$$

and for the 1D case

$$\varepsilon_2 \frac{d^2 \psi_2}{dz^2} = - \sum_{i=1}^N z_i e n_{i\infty} \exp \left(- \frac{z_i e (\psi_2 - \psi_{ref})}{k_B T} \right) \quad (70)$$

PB equation is simplified for the monovalent, $N = 2$, symmetric, $z : z$, electrolyte solution which is known as the Gouy-Chapman theory

$$\varepsilon_2 \frac{d^2 \psi_2}{dz^2} = 2 z e n_\infty \sinh \left(\frac{z e (\psi_2 - \psi_{ref})}{k_B T} \right) \quad (71)$$

Governing equations in the long-wave limit condition [29] is simplified as follows:

$$\frac{d^2 \psi_1}{dz^2} = 0 \quad (72)$$

$$\varepsilon_2 \frac{d^2 \psi_2}{dz^2} = 2 z e n_\infty \sinh \left(\frac{z e (\psi - \psi_{ref})}{k_B T} \right) \quad (73)$$

and boundary conditions

$$\psi_1 = 0 \quad \text{at } z = 0 \quad (74)$$

$$\psi_1 = \psi_2 \quad \text{at } z = h(x, y, t) \quad (75)$$

$$\varepsilon_1 \frac{d\psi_1}{dz} = \varepsilon_2 \frac{d\psi_2}{dz} \quad \text{at } z = h(x, y, t) \quad (76)$$

$$\psi_2 = \psi_{up} \quad \text{at } z = d \quad (77)$$

The following scaling parameters are defined to nondimensionalize the governing equations and the boundary conditions:

$$\Psi = \frac{ze\psi}{k_B T}, \quad Z = \frac{z}{d} \quad (78)$$

Also, a dimensionless parameter is defined, $\kappa^{-1} = \left(\frac{\epsilon_2 k_B T}{2e^2 z^2 n_\infty}\right)$, called Debye length. By using these definitions, we can rewrite equations and boundary conditions in scaled form

$$\frac{d^2 \Psi_1}{dZ^2} = 0 \quad (79)$$

$$\frac{d^2 \Psi_2}{dZ^2} = (\kappa d)^2 \sinh(\Psi - \Psi_{ref}) \quad (80)$$

and boundary conditions

$$\Psi_1 = 0 \quad \text{at } Z = 0 \quad (81)$$

$$\Psi_1 = \Psi_2 \quad \text{at } Z = \frac{h(x, y, t)}{d} = Z^* \quad (82)$$

$$\epsilon_1 \frac{d\Psi_1}{dZ} = \epsilon_2 \frac{d\Psi_2}{dZ} \quad \text{at } Z = \frac{h(x, y, t)}{d} = Z^* \quad (83)$$

Solution is as follows,

$$\Psi_1 = \frac{\Psi_s}{Z^*} Z \quad \text{at } (0 \leq Z \leq Z^*) \quad (84)$$

$$\Psi_2 = \Psi_{up} + 2 \ln \left(\frac{1 + \exp(-\kappa d(Z - Z^*)) \tanh\left(\frac{\Psi_s - \Psi_{up}}{4}\right)}{1 - \exp(-\kappa d(Z - Z^*)) \tanh\left(\frac{\Psi_s - \Psi_{up}}{4}\right)} \right) \quad \text{at } (Z^* \leq Z \leq 1) \quad (85)$$

where Ψ_s results from solution of

$$\Psi_s + \frac{\epsilon_2}{\epsilon_1} 2\kappa d \sinh\left(\frac{\Psi_s - \Psi_{up}}{2}\right) Z^* = 0 \quad (86)$$

In dimensional form

$$\psi_1 = \frac{\psi_s}{h} z \quad \text{at } (0 \leq z \leq h) \quad (87)$$

$$\psi_2 = \psi_{up} + 2 \frac{k_B T}{ze} \ln \left(\frac{1 + \exp(-\kappa(z - h)) \tanh\left(\frac{k_B T}{ze} \left(\frac{\psi_s - \psi_{up}}{4}\right)\right)}{1 - \exp(-\kappa(z - h)) \tanh\left(\frac{k_B T}{ze} \left(\frac{\psi_s - \psi_{up}}{4}\right)\right)} \right) \quad \text{at } (h \leq z \leq d) \quad (88)$$

After finding the electric potential distribution, we can calculate the net electrostatic force acting on the interface. By using definitions in Eqs. (53) and (54), the net force is given by,

$$\frac{1}{S} \vec{i}_z \cdot \vec{F}_{net} = \frac{1}{2} \epsilon_1 \left(\frac{\epsilon_1}{\epsilon_2} - 1 \right) \left(\frac{\psi_s}{h} \right)^2 \quad (89)$$

So conjoining pressure becomes [29]:

$$\phi_{ES} = -\frac{1}{2} \epsilon_1 \left(\frac{\epsilon_1}{\epsilon_2} - 1 \right) \left(\frac{\psi_s}{h} \right)^2 \quad (90)$$

Figure 5(a) shows the effects of changing the electrolytes molarity on the resultant electrostatic pressure acting on the IL-PD interface. The negative values' curves have an electric permittivity ratio ($\epsilon_r = 2.5$) and are associated with upward disjoining pressure, while the positive values' curves have an electric permittivity ratio ($\epsilon_r = 0.6$) and are associated with downward joining pressure. However, both curves experience a decay in the value of the electrostatic pressure as the interface height increases. **Figure 5(b)** outlines the effect of changing the applied voltage on the electrostatic pressure for both IL-PD bilayer and PD-PD bilayer. The electrolytic molarity and electric permittivity ratio ($\epsilon_r = 0.6$) were kept constant for all applied voltages. The graph shows that the IL-PD bilayer experiences a much larger pressure than that of the PD bilayer for the same applied voltage (Notice at $V = 10$ V).

Figure 6 shows a 2D spatiotemporal evolution for uniform electric field liquid–liquid interface instabilities, where (b) is the PD-PD bilayer and (c) is the IL-PD bilayer. When visually compared to one another, the number of pillars in the b(i) 3D representation of the PD-PD bilayer appears to be in the same order of magnitude of that of the c(i) 3D representation of the PD-IL bilayer. However, the difference between them is much higher than that since the physical domain size for PD-IL is actually 10 times smaller than that of the PD-PD. Moreover, **Figure 6** b(ii) and c(ii) confirms this size difference and shows that the average center distance between the pillars for

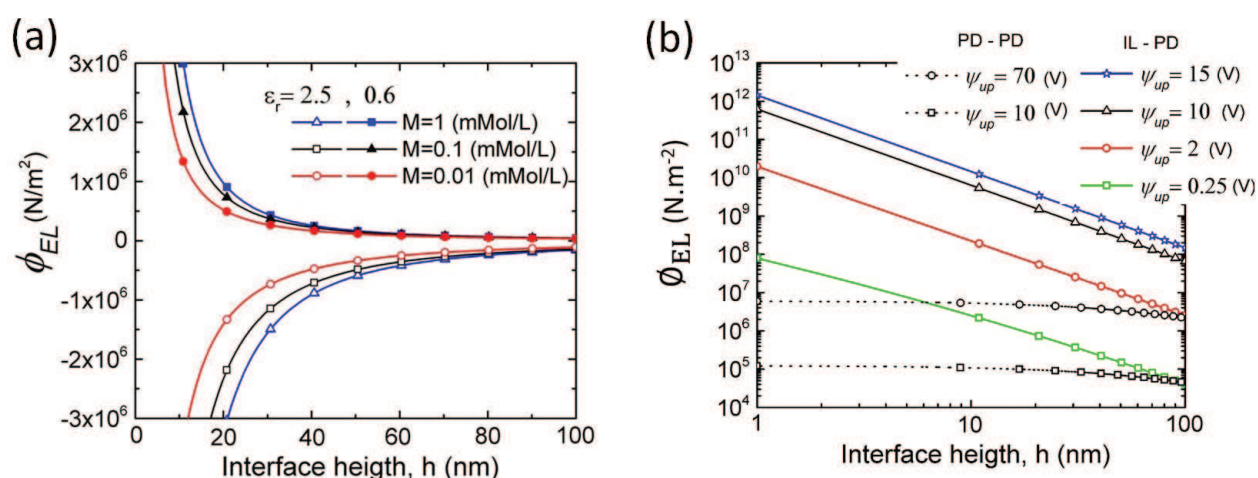


Figure 5. Electrostatic pressure distribution versus interface height. (a) Effects of electrolyte molarity in IL-PD bilayers and (b) comparison between PD-PD and PD-IL bilayers. (a) Molarity $M = 0.001, 0.0001, \text{ and } 0.00001$ mol/L and applied potential of 0.25 V and $\epsilon_1 = 2.5$. (b) $M = 0.0001$ mol/L for IL-PD, $\epsilon_1 = 2.5$ and $\epsilon_1 = 4.17$. Reprinted with permission from (HADI NAZARIPOOR et al. LANGMUIR 2014, 30, 14734–14744). Copyright (2014) American Chemical Society.

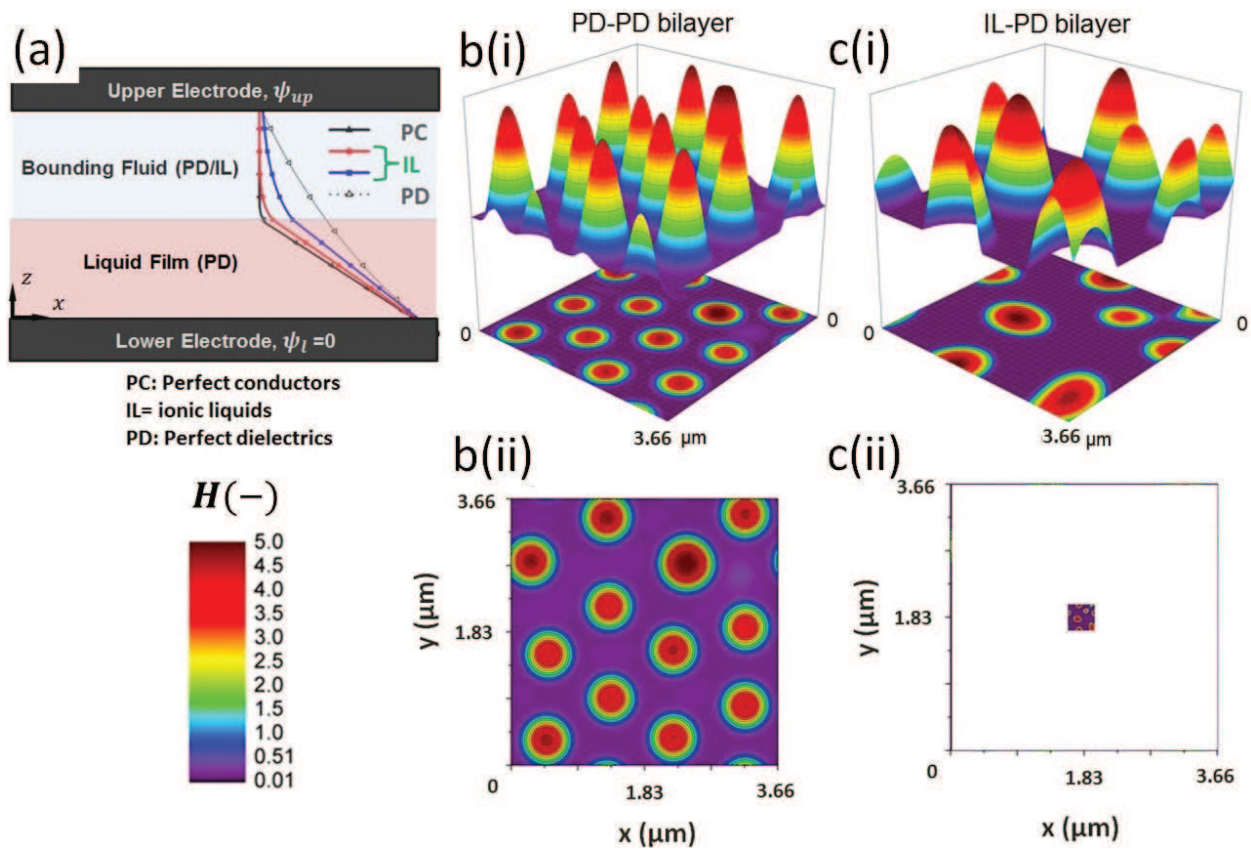


Figure 6. (a) Schematic of the IL-PD bilayer. 3D and 2D snapshots of interface morphology of (b) PD-PD, (c) IL-PD bilayer, (i) in a 3D domain, (ii) in physical domain, when $\epsilon_r = 0.6$ and $M = 100$ ($mmol/L$) for IL-PD bilayer. Initial mean film thickness is: $h_0 = 20$ nm and nondimensional time for the plots are $T =$ (b) 3.4×10^5 (c) 13.5 . $\psi_{up} = 20$ V and electric field intensities (E_0) are (a) 294 and (b) 995.

PD-IL bilayer is 210 nm while that of the PD-PD bilayer has an average center distance of 1336 nm. The formed pillars also disordered and dispersed randomly in the PD-IL case.

5. Ionic conductive film and perfect dielectric bounding media

In the previous section, the complicated case of nonlinear Poisson-Boltzmann equation Eq. (59) was considered for the IL layer. In case of low applied potential (less than 25 mV), the Debye Hückel approximation [10, 30, 31] is used to linearize the Poisson-Boltzmann equation (Eq. (80)).

$$\frac{d^2 \psi_1}{dz^2} = \kappa^2 (\psi_1 - \psi_{ref}) \quad (91)$$

and ions conservation within the layer is satisfied as follows:

$$\int_0^h \rho_f dz = \int_0^h (\psi_1 - \psi_{ref}) dz = 0 \quad (92)$$

and boundary conditions

$$\psi_1 = \psi_l \quad \text{at } z = 0 \quad (93)$$

$$\Psi_1 = \Psi_2 \quad \text{at } z = h(x, y, t) \quad (94)$$

$$\varepsilon_1 \frac{d\psi_1}{dZ} = \varepsilon_2 \frac{d\psi_2}{dZ} \quad \text{at } z = h(x, y, t) \quad (95)$$

$$\psi_2 = 0 \quad \text{at } z = 1 \quad (96)$$

where $\kappa = \left(\frac{2000 e^2 N_A M}{\varepsilon_1 \varepsilon_0 k_B T} \right)^{1/2}$ is the inverse of Debye length. Solving Eqs. (91)–(96) results in the electric potential distribution within PD and IL layers as follows:

$$\psi_2 = \left(\frac{z-d}{h-d} \right) \psi_s \quad (97)$$

$$\psi_1 = (\psi_s - \psi_l) \left[\frac{\cosh(\kappa h) + 1}{2 \sinh(\kappa h)} \right] \sinh(\kappa z) - \left(\frac{\psi_s - \psi_l}{2} \right) \cosh(\kappa z) + \frac{\psi_s + \psi_l}{2} \quad (98)$$

where ψ_s is the interface potential and is determined by the following equation:

$$\psi_s = \frac{\psi_l (1 + \cosh(\kappa h))}{1 + \cosh(\kappa h) + \frac{2\varepsilon_2}{\varepsilon_1 \kappa (d-h)} \sinh(\kappa h)} \quad (99)$$

The electrostatic pressure, in this case, is given by,

$$\phi_{EL} = \frac{1}{2} \varepsilon_2 \varepsilon_0 \left(\frac{\varepsilon_2}{\varepsilon_1} - 1 \right) \left[\frac{\psi_s}{d-h} \right]^2 \quad (100)$$

A 50-nm thick IL film surrounded by a 50 nm PD media, such as air, was considered to plot the effects of changing the electrolytic molarity have on the potential distribution across the film thickness. The plots obtained for the electric potential distribution are linear as shown in **Figure 7(a)**. For molarity (M) of 0.01 mol/L, the reduction in electric potential across the film thickness is almost zero and, thus the electric field is zero. On the other hand, the molarity of 0.00001 mol/L causes the electric potential distribution to behave similarly to a PD.

Figure 7(b) shows the changes in the electrostatic pressure and the spinodal parameter across the IL film for different molarities. The graph shows that as the molarity increases the concentration of ions increases and consequently the electrostatic pressure and its corresponding force increase. This relationship is even more significant for higher IL thicknesses. Additionally, the negative values for the pressure indicate that the forces are pushing the interface toward the upper electrode.

Figure 8(a) shows the schematic view of the IL film bounded with a PD film while **Figure 8(b)** and **(c)** compare the structural variations between a PD film and IL film. Additionally, **Figure 8(c)** emphasizes the influence of altering the film thickness on the morphology of the IL film. It is found that a faster growth of instabilities is developed by increasing the initial thickness of IL

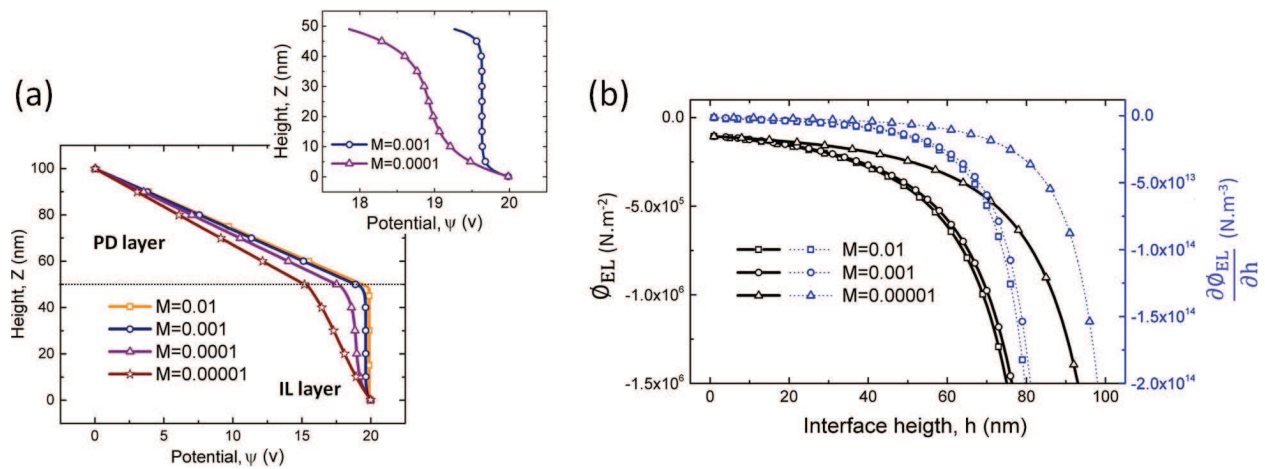


Figure 7. (a) Effect of molarity in electric potential distribution. Molarity, $M=0.01, 0.001, 0.0001,$ and 0.00001 mol/L and corresponding Debye lengths, $(\kappa)^{-1}$ are: 0.5, 1.7, 5.4, and 17 nm. (b) Electrostatic pressure, left axis, and spinodal parameter, right axis, distributions versus film thickness for three molarity values of $M=0.01, 0.001,$ and 0.00001 mol/L . $\phi_l = 20\text{ V}$, $\epsilon_1 = 2.5$ and $\epsilon_2 = 1$ [31].

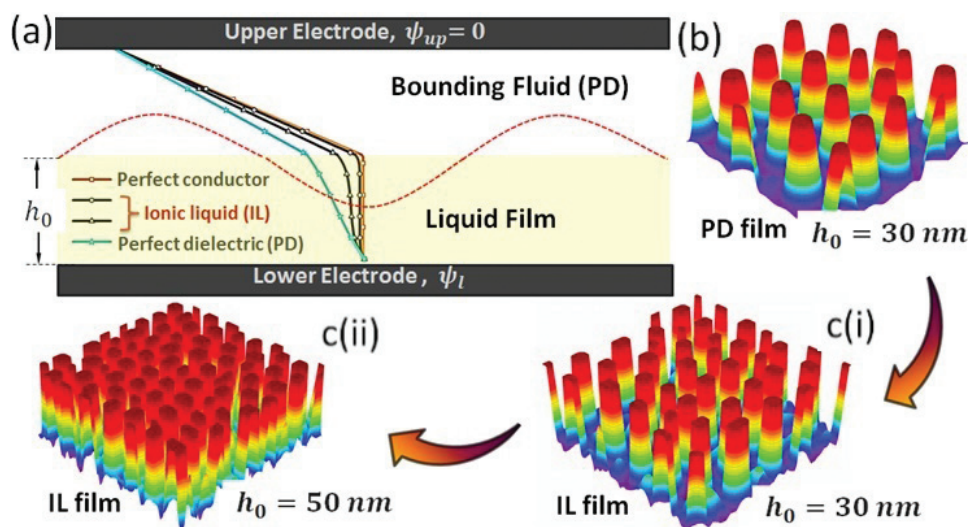


Figure 8. (a) A schematic view of the IL (film)-PD (bounding layer) bilayer and electric potential distribution. 3D snapshot of interface morphology of (b) PD film (c) IL film. Initial film thickness, $h_0 =$ (b) 30 nm (c(i)) 30 nm (c(ii)) 50 nm. $\psi_L = 20\text{ V}$ and (c) $M = 0.0001\text{ mol/L}$ [31].

film from $h_0=30$ to 50 nm, which mostly leads to more rapid patterning. On the other hand, the formed patterns are less stable as they tend to coalesce at more advanced stages.

As a way of understanding the IL films ability to make smaller sized patterns in the EHD patterning process, molarity is increased. **Figure 9** portrays the influence of molarity and the initial film thickness on the number of pillars in the EHD patterning process. In the IL film interface, the presence of large numbers of pillars indicates the creation of smaller sized pillars, given a fixed area. Changing the molarity affects the conductivity of the IL films, which in turn affect the numbers and speed of formation of the pillars. **Figure 9(a)** shows a plot of the number of pillars with respect to nondimensional time, for a PD film of the same initial

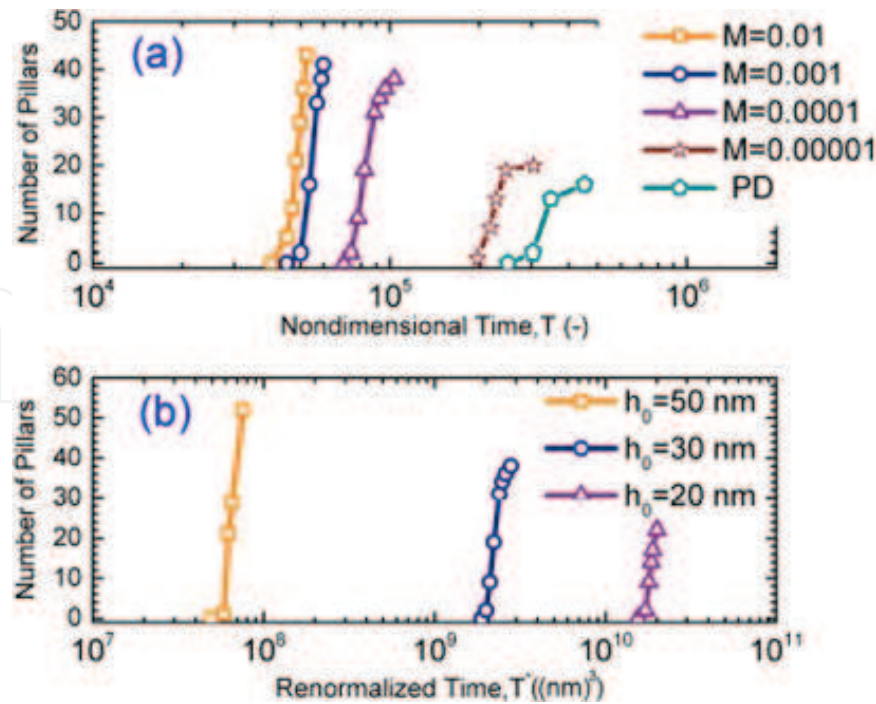


Figure 9. Number of formed pillars with (a) changes in molarity with a constant initial film thickness of $h_0=30$ nm and (b) changes in initial film thickness with a constant molarity of $M = 0.0001$ mol/L [31].

thickness, $h_0=30$ nm. The end point of each curve represents the final number of pillars formed when the quasi-stable conditions are established. As shown in **Figure 9(a)**, the final number of pillars formed for the PD film is 16, while that of the IL films is 20, 38, 41, and 43 for the following molarities, respectively: $M = 0.00001, 0.0001, 0.001, \text{ and } 0.01$ mol/L.

Therefore, one can deduce that when the molarity is initially increased by 10 times, the number of formed pillars is almost doubled. However, any further increase in molarity causes a slight increase in the number of formed pillars, finally reaching a plateau. Additionally, it can be noted that increasing the molarity decreases the time gap between the initial and final pillar formed. **Figure 9(b)** shows how the initial film thickness affects the number of pillars formed. In order to cancel the effect of changing the film thickness, nondimensional time was normalized with the initial film thickness and was plotted against the number of pillars formed, keeping the molarity constant. The results showed that the higher initial film thicknesses tend to have a faster time evolution when compared to smaller film thicknesses.

6. Conclusion

In the confined liquid layer system, the electrically induced instabilities are enlarged leading to interface deformation and pattern generation. This technique has been employed as a fast and inexpensive method for patterning of molten polymer films. In this chapter, the electrified pressure-driven instability of thin liquid films and bilayers is discussed under the long-wave approximation limit. It is shown that the difference between electrical properties of film layers

results in a net electrostatic force acting normal to the interface due to Maxwell stress. The thin film equation governs the dynamics and instability of film layers, and its derivation is discussed. An extensive numerical study is performed to generate a map, in bilayer systems, based on the filling ratio and the electric permittivity ratio of layers. This map provides a baseline for IL-PD and PD-IL bilayers and is used as a predictive model for the formation of various structures in bilayer systems. To create different morphologies with lower pattern size, the net electrostatic force is increased by introducing an ionic conductive property of liquid layers. Thus, an electrostatic model is developed to find the net electrostatic force ionic liquid films and bilayers. The developed model is integrated to the thin film equation, and the spatiotemporal evolution of the interface is presented to show the compact and smaller sized pattern formation compared to the base cases of perfect dielectric films.

Nomenclature

A	Hamaker constant
d_i	Electrodes distance, $i = 1; 2$
D	Diffusion coefficient
e	Electron charge magnitude
\vec{f}_e	External body force
F_E	Electrostatic force
F_{os}	Osmotic force
h	Interface height
h_0	Initial mean film thickness
I	Identity tensor
k_B	Boltzmann constant
l_0	Born repulsion cut off distance
L	Domain length
L_s	Scaling factor for length
m	the mobility of charges/ions
M	Molarity
\vec{n}	Normal vector to the interface
n_{\pm}	Number concentration of ions/charges, positive or negative
n^{∞}	Bulk number concentration of ions/charges

N_A	Avogadro number
P	Pressure
P_{os}	Osmotic pressure
R_{\pm}	Species production rate in chemical reactions
\vec{t}_i	Tangential vector to the interface, $i = 1$ and 2
T	Temperature
T_s	Scaling factor for time
\vec{u}_i	Velocity vector for film and bounding layer, $i = 1$ and 2
$u_{relative}$	Relative velocity
x	x direction in Cartesian coordinate
y	y direction in Cartesian coordinate
z	z direction in Cartesian coordinate

Greek Letters

s	Amplitude for growth of instabilities
ϵ_i	Electric permittivity of film and bounding layer, $i=1$ and 2
ϵ_r	Electric permittivity ratio of layers
ϵ_0	Free space electric permittivity
φ	Conjoining/disjoining pressure
φ_{Br}	Born repulsion pressure
φ_{EL}	Electrostatic pressure
Φ_s	Scaling factor for conjoining pressure
φ_T	Thermocapillary pressure
φ_{vdW}	van der Waals pressure
γ	Relative interfacial tension between film and bounding layer
κ	Inverse of Debye length
$\kappa\nu$	Wave number for growth of instabilities
κ^*	Mean interfacial curvature of the film interface

λ_{\max}	Maximum wavelength for growth of instabilities
λ	Wavelength for growth of instabilities
μ	Dynamic viscosity
ν	Kinematic viscosity
ρ	Density
ρ_f	Free charge density
ψ_i	Electric potential within the layers, $i=1$ and 2
ψ_r	Reference electric potential
ψ_l	Electric potential of the lower electrode
ψ_s	Interface electric potential
ψ_{up}	Electric potential of the upper electrode
Ψ	Nondimensional electric potential
Δt	Time step
σ	Conductivity
τ_c	Charge relaxation time
τ_p	Process time

Author details

Hadi Nazaripour*, Adham Riad and Mohtada Sadrzadeh

*Address all correspondence to: hadi@ualberta.ca

Mechanical Engineering Department, University of Alberta, Edmonton, Canada

References

- [1] Pavesi A, Adriani G, Tay A, Warkiani ME, Yeap WH, Wong SC, Kamm RD. Engineering a 3D microfluidic culture platform for tumor-treating field application. *Scientific Reports*. 2016
- [2] Shields CW, Reyes CD, López GP. Microfluidic cell sorting: A review of the advances in the separation of cells from debulking to rare cell isolation. *Lab on a Chip*. 2015;**15**(5):1230-1249
- [3] Safarnia H, Sheikholeslami M, Ganji DD. Electrohydrodynamic nanofluid flow and forced convective heat transfer in a channel. *The European Physical Journal Plus*. 2016;**131**:96

- [4] Sheikholeslami M, Chamkha AJ. Electrohydrodynamic free convection heat transfer of a nanofluid in a semi-annulus enclosure with a sinusoidal wall. *Numerical Heat Transfer, Part A: Applications*. 2016;**69**:781-793
- [5] Sheikholeslami M, Hayat T, Alsaedi A, Abelman S. Numerical analysis of EHD nanofluid force convective heat transfer considering electric field dependent viscosity. *International Journal of Heat and Mass Transfer*. 2017;**108**:2558-2565
- [6] Sheikholeslami M. Influence of coulomb forces on $\text{Fe}_3\text{O}_4\text{-H}_2\text{O}$ nanofluid thermal improvement. *International Journal of Hydrogen Energy*. 2017;**42**(2):821-829
- [7] Teubner M. The motion of charged colloidal particles in electric fields. *The Journal of Chemical Physics*. 1982;**76**(11):5564-5573
- [8] de Ven, Van and T. G., M.. *Colloidal Hydrodynamics*. San Diego, CA: Academic Press; 1989
- [9] Ning W, Russel WB. Micro- and Nano-patterns created via Electrohydrodynamic instabilities. *Nano Today*. 2009;**4**:180-192
- [10] Gambaryan-Roisman T. Modulation of Marangoni convection in liquid films. *Advances in Colloid and Interface Science*. 2015;**222**:319-331
- [11] Mukherjee R, Sharma A. Instability, self-organization and pattern formation in thin soft films. *Soft Matter*. 2015;**11**:8717-8740
- [12] Hong H, Tian H, Shao J, Ding Y, Jiang C, Liu H. Fabrication of bifocal microlens arrays based on controlled electrohydrodynamic reflowing of pre-patterned polymer. *Journal of Micromechanics and Microengineering*. 2014;**24**:095027
- [13] Li H, Yu W, Wang Y, Bu H, Liu Z, Abraham E, Desmulliez MPY. Simulation of the electrohydrodynamic instability process used in the fabrication of hierarchic and hollow micro/nanostructures. *RSC Advances*. 2014;**4**:13774-13781
- [14] Hu H, Tian H, Li X, Shao J, Ding Y, Liu H, An N. Biomimetic mushroom-shaped microfibers for dry adhesives by electrically induced polymer deformation. *ACS Applied Materials & Interfaces*. 2014;**6**:14167-14173
- [15] Atta A, Crawford DG, Koch CR, Bhattacharjee S. Influence of electrostatic and chemical heterogeneity on the electric-field-induced destabilization of thin liquid films. *Langmuir*. 2011;**27**(20):2472-2485
- [16] Oron A, Davis SH, Bankoff SG. Long-scale evolution of thin liquid films. *Review of Modern Physics*. 1997;**69**:931-980
- [17] Israelachvili JN. *Intermolecular and Surface Forces*. Burlington, MA: Academic Press; 2011
- [18] Masliyah JH, Bhattacharjee S. *Electrokinetic and Colloid Transport Phenomena*. Hoboken, NJ: Wiley-Interscience; 2006

- [19] Vladimir SM. Dewetting of solid surface: Analogy with Spinodal decomposition. *Journal of Colloid and Interface Science*. 1993;**156**:491-497
- [20] Harlow FH, Eddie Welch J. Numerical calculation of time-dependent viscous incompressible flow of fluid with free surface. *Physics of Fluids*. 1965;**8**:2182-2189
- [21] Hirt CW, Nichols BD. Volume of fluid (VOF) method for the dynamics of free boundaries. *Journal of Computational Physics*. 1981;**39**:201-225
- [22] Craster RV, Matar OK. Electrically induced pattern formation in thin leaky dielectric films. *Physics of Fluids (1994-present)*. 2005;**17**:1131-1198
- [23] Verma R, Sharma A, Kargupta K, Bhaumik J. Electric field induced instability and pattern formation in thin liquid films. *Langmuir*. 2005;**21**(8):3710-3721
- [24] Tian H, Shao J, Ding Y, Li X, Liu H. Numerical characterization of electrohydrodynamic micro- or nanopatterning processes based on a phase-field formulation of liquid dielectrophoresis. *Langmuir*. 2013;**29**(15):4703-4714
- [25] Yang Q, Li BQ, Ding Y. A numerical study of nanoscale electrohydrodynamic patterning in a liquid film. *Soft Matter*. 2013;**9**:3412-3423
- [26] Hadi N. *Electrohydrodynamic and Thermocapillary Instability of Thin Liquid Films* [thesis]. University of Alberta: University of Alberta; 2016
- [27] Nazaripoor H, Koch CR, Sadrzadeh M, Bhattacharjee S. Thermo-Electrohydrodynamic patterning in Nanofilms. *Langmuir*. 2016;**32**(23). DOI: 10.1021/acs.langmuir.6b01810
- [28] Nazaripoor H, Koch CR, Sadrzadeh M. Enhanced electrically induced micropatterning of confined thin liquid films: Thermocapillary role and its limitations. *Industrial & Engineering Chemistry Research*. 2017;**56**. DOI: 10.1021/acs.iecr.7b02814
- [29] Nazaripoor H, Koch CR, Bhattacharjee S. Electrical perturbations of ultrathin bilayers: Role of ionic conductive layer. *Langmuir*. 2014;**30**(49):14734-14744. DOI: 10.1021/la503839x
- [30] Nazaripoor H, Koch CR, Sadrzadeh M, Bhattacharjee S. Compact micro/nano electrohydrodynamic patterning: Using a thin conductive film and a patterned template. *Soft Matter*. 2016;**12**(4)
- [31] Nazaripoor H, Koch CR, Sadrzadeh M, Bhattacharjee S. Electrohydrodynamic patterning of ultra-thin ionic liquid films. *Soft Matter*. 2015;**11**(11):2193-2202

